

pubs.acs.org/NanoLett Letter

Reduced-Dimensionality Al Nanocrystals: Nanowires, Nanobars, and Nanomoustaches

David Solti, Christian R. Jacobson, J. Alexander Orion Yates, Benjamin Franklin Hammel, Gopal Narmada Naidu, Catherine E. Arndt, Aaron Bayles, Yigao Yuan, Parmeet Dhindsa, Jessica T. Luu, Corbin Farr, Gang Wu, Henry O. Everitt, Ah-Lim Tsai, Sadegh Yazdi, Peter Nordlander,* and Naomi J. Halas*



Cite This: Nano Lett. 2024, 24, 6897-6905



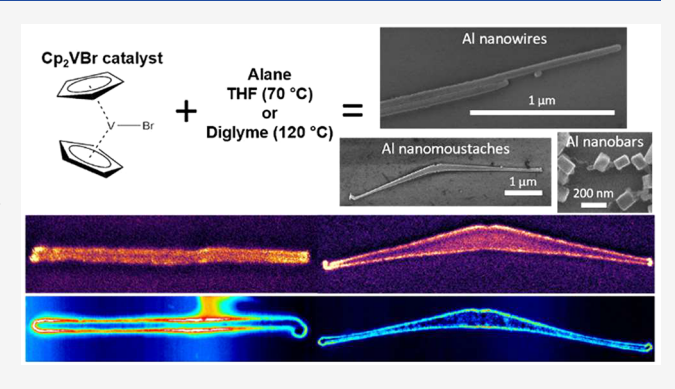
ACCESS

III Metrics & More

Article Recommendations

Supporting Information

ABSTRACT: Aluminum nanocrystals created by catalyst-driven colloidal synthesis support excellent plasmonic properties, due to their high level of elemental purity, monocrystallinity, and controlled size and shape. Reduction in the rate of nanocrystal growth enables the synthesis of highly anisotropic Al nanowires, nanobars, and singly twinned "nanomoustaches". Electron energy loss spectroscopy was used to study the plasmonic properties of these nanocrystals, spanning the broad energy range needed to map their plasmonic modes. The coupling between these nanocrystals and other plasmonic metal nanostructures, specifically Ag nanocubes and Au films of controlled nanoscale thickness, was investigated. Al nanocrystals show excellent long-term stability under atmospheric conditions, providing a practical alternative to coinage metal-based nanowires in assembled nanoscale devices.



KEYWORDS: aluminum nanocrystals, nanowires, nanomoustaches, plasmonics, cathodoluminescence, electron energy loss spectroscopy

Reduced-dimensionality nanocrystals, such as nanowires, are of substantial interest for applications that include optical computing, 1,2 electronic devices, 3,4 and chemical catalysis. 5-7 They are considered to be important building blocks of nanotechnology due to their excellent physicochemical properties.^{8,9} Resonant illumination of a metallic nanoparticle can excite the collective oscillatory modes of free electrons, known as localized surface plasmon resonances (LSPRs). The LSPRs of large-aspect-ratio metallic nanocrystals have discrete longitudinal and transverse modes that can be selectively optically excited by specific wavelength and polarization combinations and collectively excited by an electron beam. Au, Ag, and Cu nanowires have all been synthesized to date and all have certain limitations. Au and Cu nanowires are lossy in the visible frequency range due to dband electronic transitions; 10,111 Ag nanowires 12-18 are readily oxidized upon ambient exposure over a few days, limiting reproducibility of their properties in device contexts. Development of a robust plasmonic nanowire without these limitations could facilitate an increased interest in plasmonic nanodevice development.

Aluminum has recently emerged as an Earth-abundant, sustainable alternative to coinage metals in nanoparticle synthesis. Al nanocrystals possess a self-limiting native surface oxide, preventing ambient oxidation.²⁰ Al supports LSPRs that

can be excited by light spanning the deep ultraviolet, the visible, and into the infrared wavelength range,²⁰ and lacks the strong absorptive losses associated with the interband transitions in the d-band metals Au and Cu.²¹ The use of lithographically patterned Al nanostructures for plasmonic applications has been limited by the multicrystalline nature and uncontrolled oxide content of Al films that forms during film growth.^{22,23} These characteristics motivate research interest in the chemical synthesis of Al nanocrystals with large-aspectratio morphologies.

Al nanowires have been grown using thermal substitution, ²⁴ chemical vapor deposition, ²⁵ sputtering, ²⁶ template-assisted growth methods, ²⁷ and by solution phase synthesis. ^{28,29} Recently, the catalyzed decomposition of alane (AlH₃) with a Ti-center, cyclopentadienyl ligand-bearing molecular catalyst was shown to provide a useful strategy for morphology-controlled Al nanocrystal growth. ^{30–32} The catalyst ligands

Received: February 20, 2024 Revised: May 20, 2024 Accepted: May 21, 2024 Published: May 28, 2024





Nano Letters pubs.acs.org/NanoLett Letter

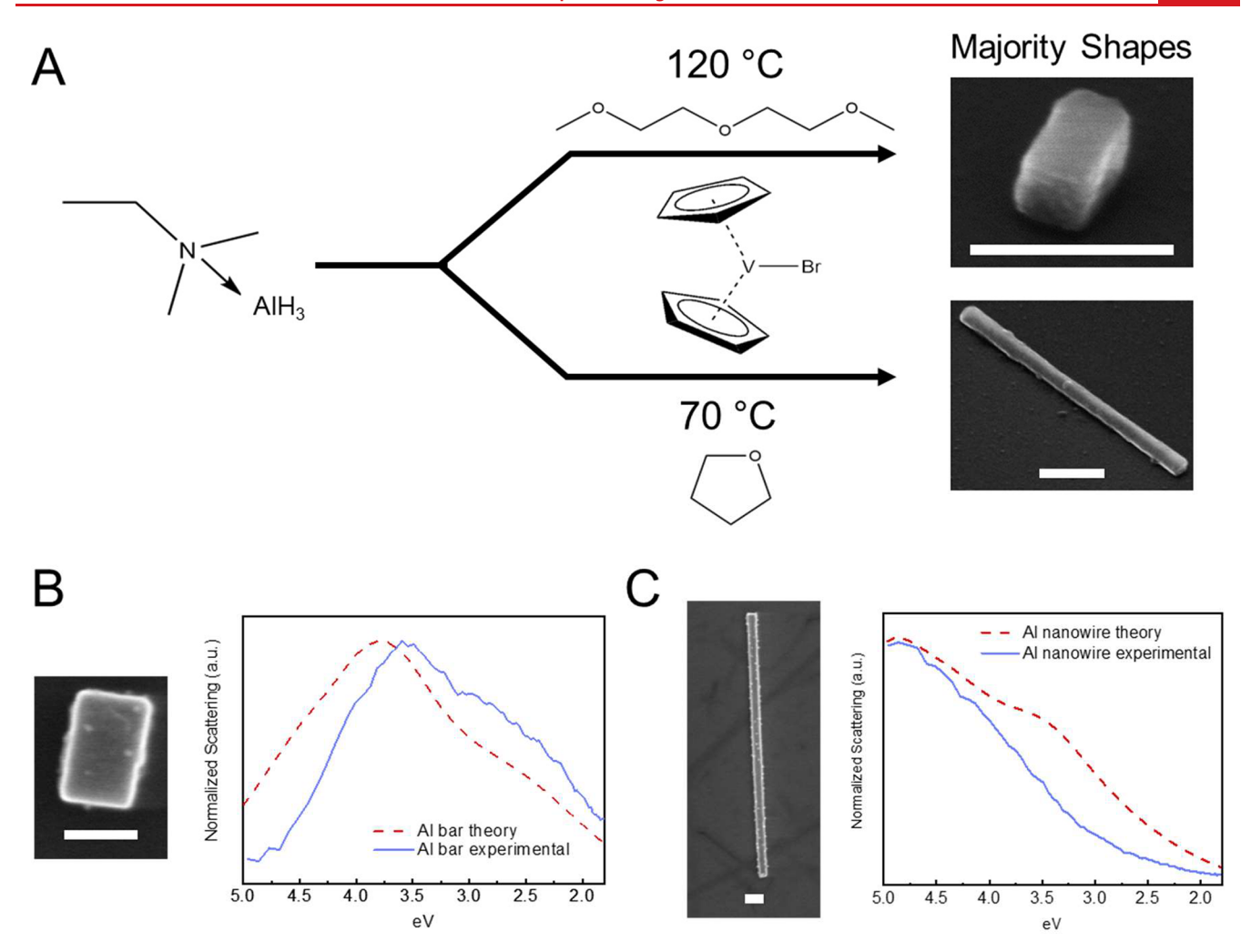


Figure 1. (A) Synthesis of Al nanobars and Al nanowires produced through the Cp_2VBr -catalyzed decomposition of alane, with corresponding single-particle SEM micrographs of the major product of each synthesis. Scale bars = 250 nm. (B) Single Al nanobar on glass substrate with the corresponding darkfield scattering spectrum (blue) and FDTD simulation (dashed red). (C) Single Al nanowire on glass substrate with the corresponding darkfield scattering spectrum (blue) and FDTD simulation (dashed red). Scale bars = 100 nm for (B, C).

were shown to passivate specific index surfaces of the growing nanocrystals, resulting in single crystal Al nanocrystal morphologies with preferential growth along specific index faces. ^{30,32,33} Further increasing the Al nanocrystal anisotropic growth, however, requires strategies beyond catalyst ligand passivation. We can invoke the Sabatier principle ³⁴ from heterogeneous catalysis, where we balance the relative binding affinities of the reactant and product to the catalyst. Adopting this principle for Al nanocrystal synthesis, overall reaction rates should be reduced if either reactant or product binding constants are too strong. Changing the catalyst metal from Ti to a metal with a stronger binding affinity to Al should facilitate the growth of strongly anisotropic nanocrystals by reducing the growth rate.

Here we report the colloidal synthesis of Al nanowires, nanobars, and nanomoustaches. Strongly anisotropic nanocrystal growth is achieved by changing the catalyst metal from Ti to V: from Tebbe's reagent to bis(cyclopentadienyl)-vanadium(III) bromide (Cp₂VBr). This catalyst drastically slows the reaction rate relative to Ti-based catalysts while maintaining the surface affinity of the cyclopentadienyl catalyst ligands for the growing nanocrystal. The nanocrystals display exceptional stability under ambient conditions even one year

after synthesis, preserving their plasmonic behavior. Plasmon mapping of Al nanowires through electron energy loss spectroscopy (EELS) confirms that they support multiple longitudinal plasmon modes, with the strongest modes in the infrared (IR) region and higher order resonances extending through the visible region and into the ultraviolet. Due to being an electronic excitation, EELS captures both the radiative and nonradiative plasmon decay processes, allowing for visualization of dark modes. Additionally, the optical properties of the nanobars and nanowires were characterized using dark-field microspectroscopy of individual nanocrystals. We studied the plasmonic characteristics of Al nanowires coupled to Au films of increasing thicknesses to examine plasmon coupling via virtual state interactions in this geometry. We also investigated the coupling of Ag cubes with Al nanowires, monitoring their cathodoluminescence (CL), and demonstrating remote excitation of bright modes in this mixedmetal system. These studies demonstrate the integration of chemically synthesized, reduced-dimensionality Al nanocrystals with other plasmonic metals into a variety of plasmonic geometries.

Al nanowires, nanobars, and nanomoustaches were grown under Ar atmosphere in a glovebox using a vanadium complex,

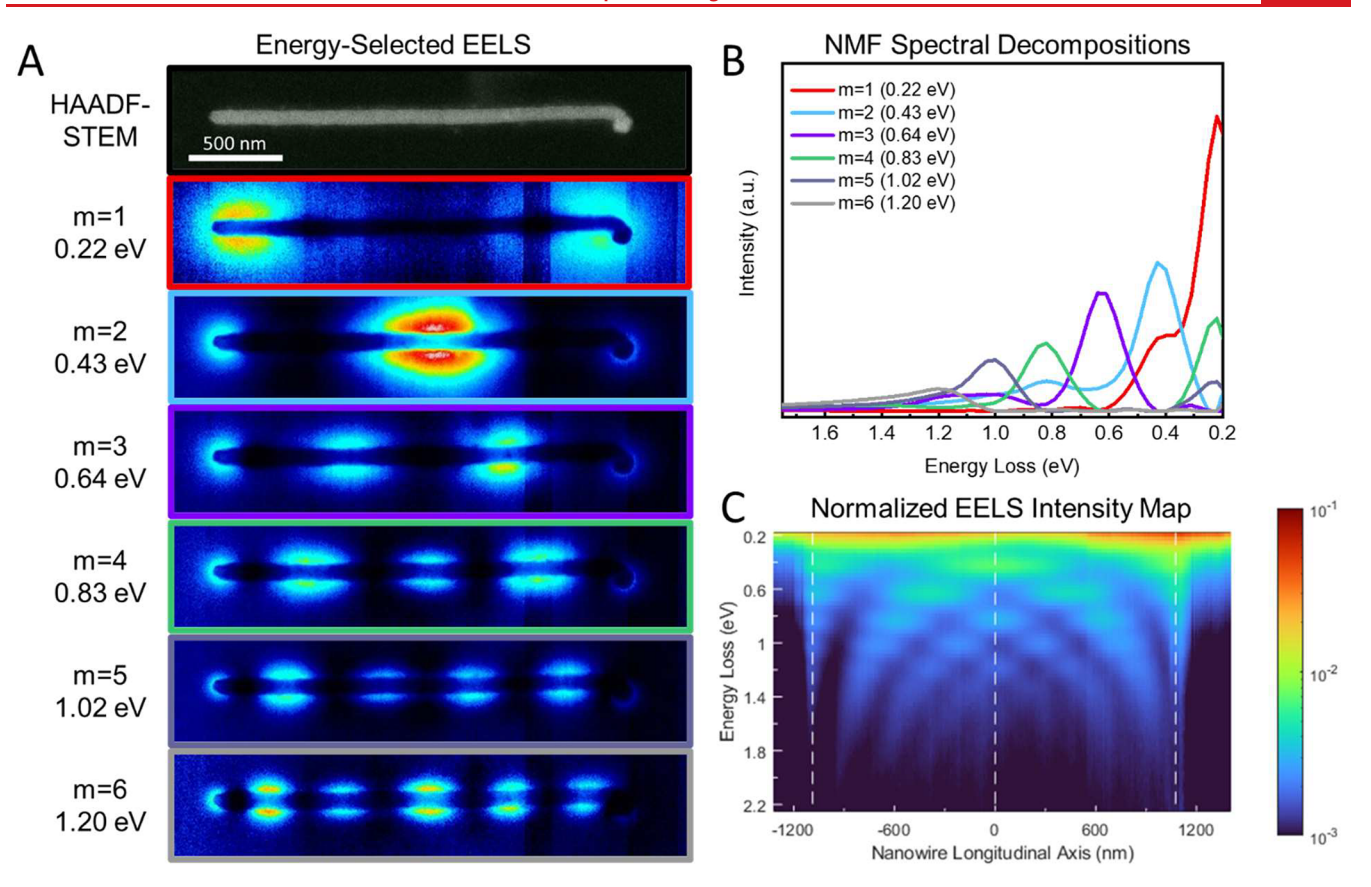


Figure 2. EELS plasmon mapping of an Al nanowire. (A) LSPR maps and (B) their corresponding spectral components extracted by the NMF method from EEL spectrum images. (C) EELS intensity map from the same Al nanowire, showing the discrete energy modes observed. The intensity map is calculated by averaging the EEL spectrum along the nanowire width. The EELS data are cropped from 0.18 to 2.25 eV for visualization purposes only.

Cp₂VBr, which decomposed alane catalytically at a slower rate than reported for Al nanocrystal growth using Ti-based catalysts (Figure 1a). 30,33 The catalytic behavior of Cp₂VBr was observed through electron paramagnetic resonance (EPR) spectroscopy, and the V3+ center lost all EPR signal upon addition of AlH₃ (Figure S1). The observation of V³⁺ X-band EPR signals in Cp₂VBr suggests very small zero-field splitting between the two 3d electrons, and the elimination of the signals upon its reaction with AlH3 indicates that a strong electronic bond is formed between the two molecules. The slower growth rate was also observed through inductively coupled plasma mass spectrometry (ICP-MS), where the quantification of atomic Al from time-stopped experiments demonstrated a greatly reduced rate of Al particle formation (Figure S2). Previously studied Al NC syntheses incorporating a Ti-centered catalyst 30,32,33 typically completed within hours, while the V-catalyzed Al nanowire reaction typically occurred over nominally 24 h.

Cooling the reaction temperature from 120 to 70 °C allows for tuning from cubic and bar morphologies to Al nanowires (Figure 1a). Diglyme was selected as the nanobar reaction solvent to allow for the increased reaction temperatures, similar to a previously published synthesis.³¹ Nanowires were grown using anhydrous, unstabilized tetrahydrofuran, which was the solvent that supported the best solubility of the vanadium catalyst. The majority products of each reaction were single crystalline anisotropic nanobars (42.6%) or nanowires (36.5%) (Figure 1a, right). For Al nanobar reactions, cubes (14.7%), right bipyramids (16.1%), and penta-twinned rods (6.3%) were

also present, as in previous studies. 9,30 In Al nanowire reactions, small cubes and bars (18.8%, combined), singly twinned wires named "nanomoustaches" (1.9%), and 2D nanodiamonds (9.9%) were also obtained. Both the nanobar and nanowire syntheses also resulted in a minority of poorly formed structures (20.3% and 32.9%, respectively). A detailed summary of the various morphologies present is provided (Figure S3). Corresponding SEM micrographs of the minority products are also shown (Figure S4). The presence of particlewire fused hybrids (Figure S5) in the Al nanowire reactions indicates that oriented attachment may be the likely growth method, an observation that merits further detailed study, which would require the analysis of reaction outcomes at early time points under rigorously nonoxidative conditions.

High-resolution transmission electron microscopy (TEM) images of Al nanobars and nanowires show their characteristic 3–5 nm amorphous Al_2O_3 layer, which protects the metallic Al crystal from further oxidation (Figure S6). High-angle annular dark-field scanning transmission electron microscopy (HAADF-STEM) imaging was used in conjunction with energy-dispersive X-ray spectroscopy to map the elemental Al and O signals of the grown Al nanowires and nanobars, confirming surface oxide growth (Figure S7). The average size of the grown Al nanobars was 124 nm \times 91 nm (with standard deviations of 19 and 17 nm, respectively). The Al nanowires had an average size of 3466 nm \times 113 nm, with their lengths varying from 345 nm to over 23 μ m (Figure S3).

Single-particle dark-field microspectroscopy was performed on individual Al nanobars (Figure 1b) and nanowires (Figure

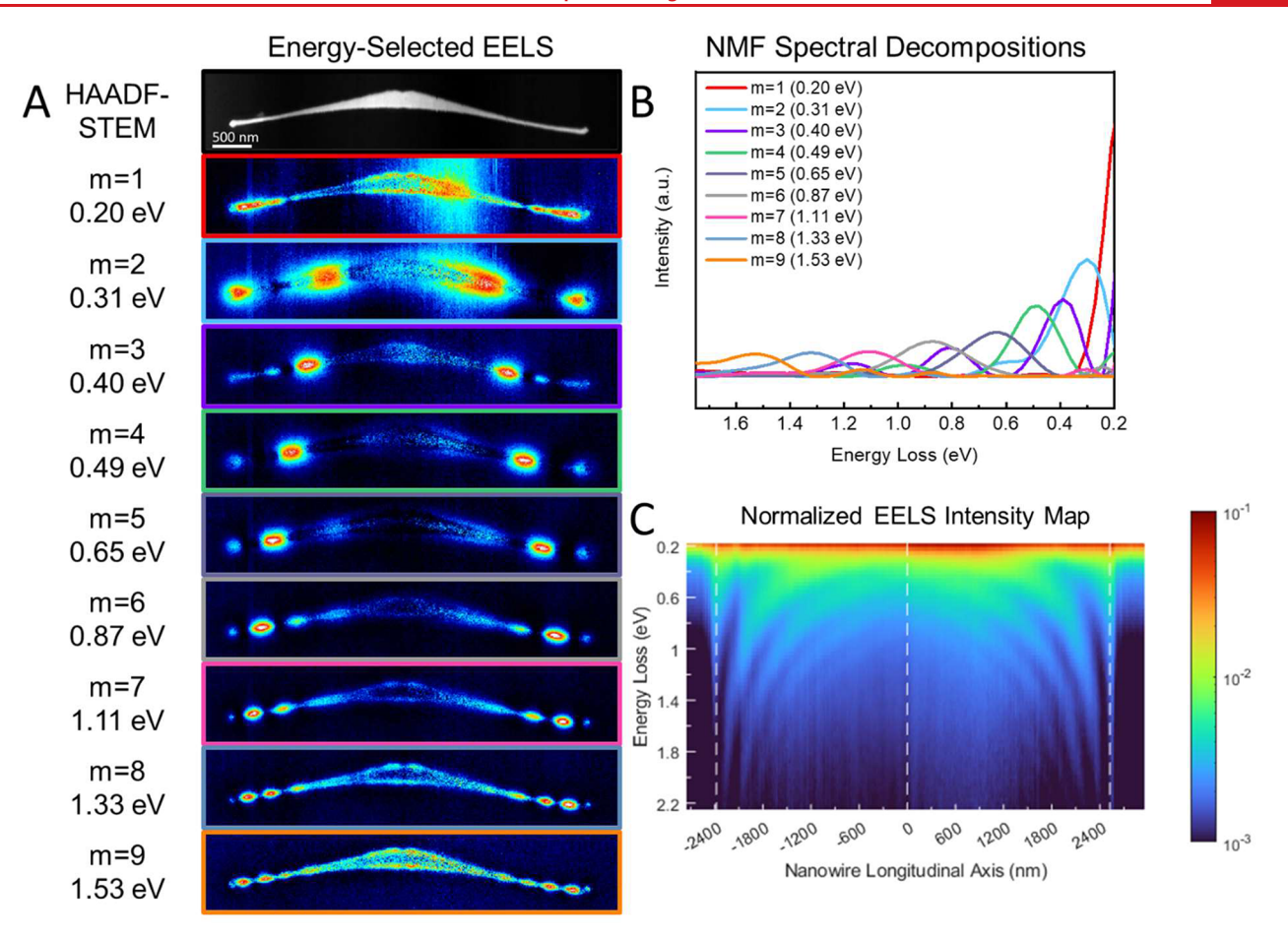


Figure 3. EELS plasmon mapping of an Al nanomoustache. (A) An example of LSPR maps and (B) their corresponding spectral components extracted by the NMF method with 9 components from EEL spectrum images. (C) EELS intensity map from the same Al nanomoustache, showing continuous energy modes from IR at 0.2 eV up to visible at about 2 eV. The intensity map is calculated by averaging the EEL spectrum along the nanomoustache width. The EELS data is cropped from 0.18 to 2.25 eV for visualization purposes only.

1c), where the spectra obtained were found to agree well with finite-difference time domain (FDTD) calculations of the same nanoparticle morphologies with the same optical excitation and collection geometries used in the experiment. The Al nanowires were found to have strong ultraviolet features for transverse excitation, with the dipolar plasmon mode present at \sim 3.5 eV and a strong quadrupolar mode near \sim 5.0 eV. The nanobars were similar to previously characterized Al nanocubes, 30 with a visible dipolar plasmon at \sim 2.7 eV seen as a shoulder and a strong quadrupolar plasmon present near \sim 3.6 eV.

To investigate the plasmonic properties of Al nanowires, monochromated STEM-electron energy loss spectroscopy (EELS) on individual nanowires and nanomoustaches was conducted. Experimental data were gathered by scanning a focused, monochromated 80 keV beam with an energy resolution of 100 meV (zero-loss peak FWHM) over the nanocrystal of interest and recording both HAADF images and EELS maps. We confirmed the metallic characteristics of the synthesized Al nanowires through observation of the bulk Al plasmon at nominally 15 eV (Figures S8, S9). In all cases, the samples that were imaged retained their metallic core without degradation or special storage for over one year. The spatial distribution of LSPR modes was extracted using non-negative matrix factorization (NMF)^{35,36} from the spectral images acquired by STEM-EELS (Figure 2a,b). We note that the

FWHM of NMF-extracted peaks cannot be directly compared due to their non-Gaussian nature. The intensity maps in Figure 2c show the raw electron energy-loss spectra, normalized by the zero-loss peak intensity and averaged along the short axis of the nanocrystals as a function of position along their long axes (see Supporting Information and Figure S10).

In the case of the Al nanowire, a Fabry-Pérot type standing wave pattern is present for modes m = 1-6 as seen in the EELS studies of coinage metal nanowires. 37-39 Similar to other studies on the optical properties of aluminum nanostructures, we also observed the bulk plasmon peak at 15 eV and a broad peak at 6.9 eV corresponding to the electrostatic plasmon (Figure S8).40,41 Multiple discrete resonance modes are imaged along the length of the nanowire, similar to those in Ag nanowires.³⁸ The mapped plasmon fields radiate most strongly for the lower-energy modes. We measured the decay length of the EELS signal to evaluate the extent of the evanescent field (Figure S11). The measured decay lengths for 0.43, 0.64, 0.83, 1.02, and 1.2 eV modes were 145, 110, 77, 55, and 44 nm, respectively. These decay lengths are comparable to those measured for Ag nanowires.³⁷ For the lowest energy modes, the plasmonic peaks radiate hundreds of nanometers from the Al nanowire. A non-NMF-based EELS intensity map was generated (Figure 2c) to confirm the identified plasmonic features. This intensity map aligns quite closely with our NMF-

based energy selections, reinforcing our identification of discrete nanowire plasmon modes.

We also studied the Al nanomoustache using monochromated EELS (Figure 3). To our knowledge, no other colloidally synthesized nanocrystal has demonstrated such a uniform, continuous diameter variation over a multiple-micrometer length scale. The Al nanomoustache shows almost perfect mirror symmetry with respect to the singly twinned domain boundary at its center, providing a unique opportunity to examine the EELS LSPR mapping of Al nanowires across curvature, thickness, and twinning variances.

The EELS LSPR maps of the nanomoustache (Figure 3a) also show Fabry-Pérot type resonances extending from the IR (0.20 eV) into the visible region of the spectrum (1.54 eV). Typical higher-energy plasmon modes are observed in UV as well (Figure S9). The standing waves occur throughout the curvature and diameter variance of the Al nanomoustache. However, NMF decomposition (Figure 3b) suggests a continuous, overlapping set of peak intensities distinct from the discrete modes observed for Al nanowires (Figure 2b). The energy and position of the plasmon peaks in the nanomoustache extracted using the NMF decomposition are ambiguous and depend on the number of NMF spectral components selected for fitting. In Figure 3a and b, we show an example of LSPR maps for 9 spectral components, where additional local excitations, internal to the nanomoustache, can be observed for all 9 modes. As can be seen in Figure 3B, the modes overlap strongly with each other. For this morphology, NMF is therefore unable to unambiguously identify discrete modes, most likely because of the continuous gradient in the nanomoustache diameter along its length. The strong dependence of peak positions on the number of modes as well as the appearance of additional local excitations suggests a continuum of peak energies and positions. This observation is reinforced by the EELS intensity map shown in Figure 3c, indicating a continuous pattern of modes maintained for all resonant energies rather than discrete modes typical of standing waves. When compared to the discrete energy distribution of the nanowire (Figure 2c), the absence of similar discrete energy levels is clearly apparent for the Al nanomoustache (Figure 3c). The diameter gradient of the Al nanomoustache introduces different interference conditions, which results in a continuous pattern of modes. We further probed whether this distribution present in the raw EELS is from the peaks shifting in energy or spatial domains (Figure S27). As EELS data were gathered farther from the tips toward the thicker portions of the center, the spectra significantly red-shifted, but the LSPR peaks are clearly separated in the energy domain. Therefore, we attribute the continuous energy shift observed to the local thicknesses changing along the length of the nanomoustache wire, thus changing the plasmonic response to electronic stimuli.

The scattering properties of Al nanowires in the visible region of the spectrum allow for studies of coupled plasmon behavior with other plasmonic metals. The coupling between individual Al nanowires and plasmonic Au films of thicknesses 30, 60, 120, 240, and 1000 nm was studied using visible-NIR dark-field microspectroscopy (Figure 4). Because conical white-light excitation was used, the collected dark-field scattered light was filtered through a linear polarizer in 10° increments from $0^{\circ}-180^{\circ}$. Scattered light perpendicular to the nanowire is defined as transverse (Figure 4a), and light parallel to the nanowire as longitudinal (Figure S12). A two-dimensional theoretical model was developed to better

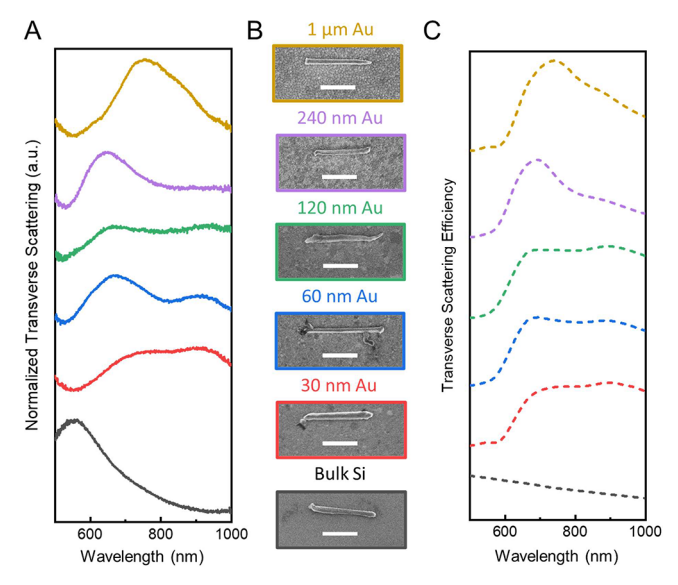


Figure 4. (A) Normalized transverse-polarized experimental darkfield scattering spectra of Al nanowires on Au films of thickness 0 (black, Si), 30 (red), 60 (blue), 120 (green), 240 (purple), and 1000 (yellow) nm. (B) Correlated SEM micrographs of the particles from which each spectrum was collected are shown. All scale bars are 1000 nm. (C) Theoretical scattering spectra for an ovular Al cylinder placed on top of Au films of thicknesses 0, 30, 60, 120, 240, and 1000 nm. The semimajor and semiminor axes are 77 nm \times 72 nm, 77 nm \times 55 nm, 63 nm \times 53 nm, 63 nm \times 55 nm, 60 nm \times 40 nm, and 70 nm \times 41 nm, respectively. All axis lengths include a 5 nm alumina layer.

understand the evolution of the spectral features with film thickness observed in the experimental data (COMSOL Multiphysics 5.4). The model consists of an Al nanowire surrounded by a 5 nm Al oxide layer atop a variable-thickness Au layer on a semi-infinite silicon substrate. The dielectric functions used for Al, Al_2O_3 , Au, and Si were obtained from literature values. Figures S13 and S14 show theoretical spectra for wires with a circular cross section and a radius of 77 nm, including the alumina layer.

Since all of the nanowires imaged show visible thickness deviations from a constant, circular cross section along their lengths, we assume that those inhomogeneities dominate their transverse scattering properties. To take this into account, the nanowires were described as having an elliptical cross section. The lengths of the semimajor and semiminor axes are taken as free parameters to match the experimental data. For all wires, the semiminor axis is oriented normal to the substrate.

For a nanowire positioned on a Si substrate with no Au film present, a single Al nanowire peak is observed at ~600 nm (Figures 4a, part b, black). This peak is the Si-screened dipole resonance. The calculated transverse scattering spectrum of the Al nanowire decreases monotonically with increasing wavelength between 500 and 1000 nm (Figures 4c, S13). Furthermore, the thickness of the Al nanowire greatly shifts the observed dipole resonance (Figure S28).

For an Al nanowire positioned onto a thin layer of Au (30 or 60 nm), the nanowire—film interaction gives rise to an effective continuum at energies lower than those of the transverse dipolar plasmon of the Al nanowire. In this case, the higherenergy hybridized plasmon (650–700 nm) results from a quasi-bound state in the continuum composed primarily of the nanowire plasmon, red-shifted due to its interaction with the film (Figures 4a,c and S13; red and blue). The broad density of

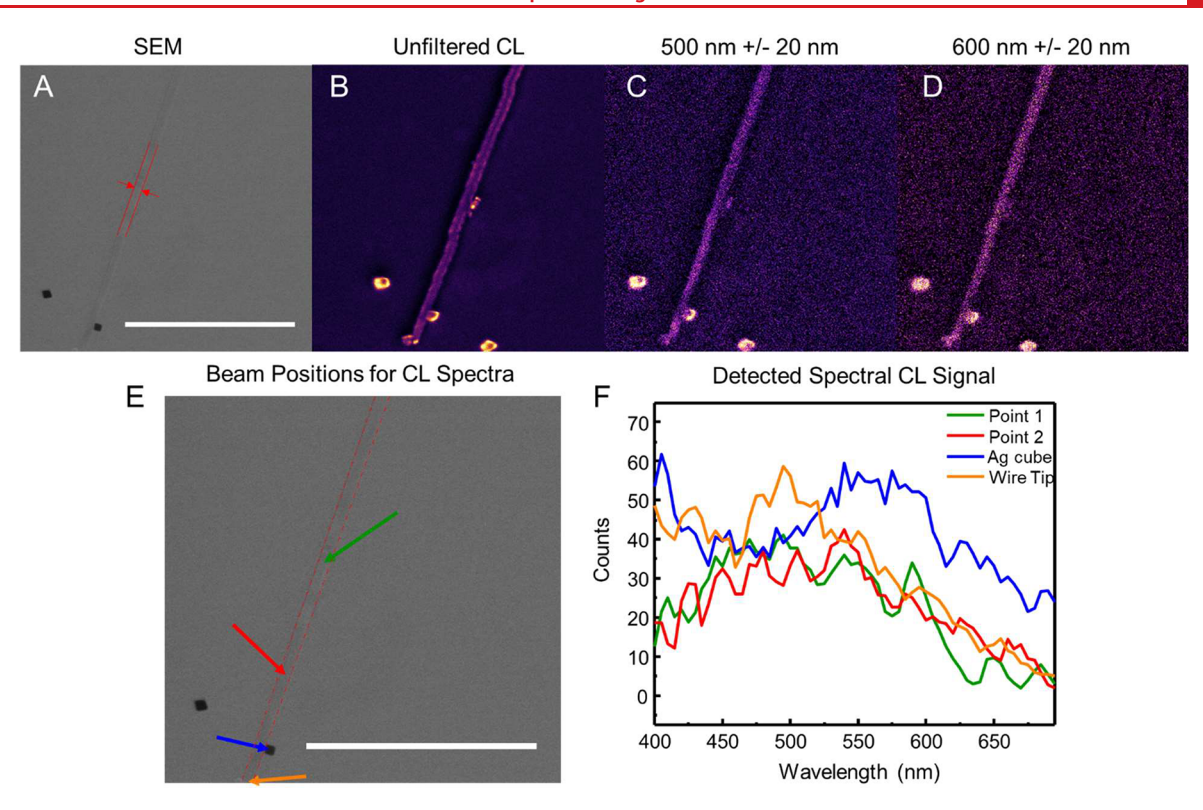


Figure 5. Cathodoluminescent panchromatic imaging of an Al nanowire-Ag nanocube coupled system. All filtered CL images were uniformly brightened by 40% to aid in identification of regions of interest. (A) SEM image of an Al nanowire coupled to a single Ag nanocube on a SiN grid. Red markings highlight location of Al nanowire. SEM image without markings is shown in Figure S25. (B) Unfiltered CL map, (C) 500 nm bandpass filtered map, and (D) 600 nm bandpass filtered map of the same nanowire–nanocube system. Brighter (more yellow) colors indicate a higher intensity of light detected. (E) SEM micrograph (red markings indicate location of Al nanowire) depicting the approximate area where the electron beam was placed to excite the Al nanowire–Ag nanocube system (see Figure S26 for raw beam-placement data), and (F) corresponding CL spectra from each of the 4 points. Scale bars are 2 μ m.

states of the Al nanowire, compounded by its slight irregularities in shape and width, limits this resonance from being a true bound state in the continuum. The peak observed at longer wavelengths (900–1000 nm) is due to a virtual resonance⁴⁷ of the Au film, caused by the collective excitation of all propagating surface plasmons in the Au layer whose wavelengths are longer than twice the nanowire's width (Figure 4a,c, red, blue). A more detailed discussion of the virtual resonance, including a virtual state calculation on an adapted Al particle-Au film system using a previously reported method,⁴⁷ is presented in the Supporting Information (Figures S15–S20).

When the Au film thickness is increased to 120 nm and above, the Al nanowire transverse plasmon interacts with a perfect image charge within the Au film, yielding a resonance at ~650 nm (Figure 4, green, purple, and yellow). Here, the thicker Au films lie within the semi-infinite limit. The nanowire still couples to propagating surface plasmons in the Au layer in this limit, so we still observe the virtual state as a broad spectral feature at longer wavelengths (800-100 nm). The Al nanowire-perfect image charge dimer has a higher energy than the virtual resonance, consistent with experimental observations. Changes in nanowire length from ~2000 to ~3500 nm did not qualitatively affect observed experimental resonances, confirming that the observed nanowire-film coupling is due to the transverse nanowire plasmon modes (Figure S21). Further observations in changing an Al cylinder's length from 100 to 300 nm and to an infinite length show the transverse dipole being broadened (Figure S29).

We also investigated the remote excitation of Ag nanocubes by plasmons launched on individual Al nanowires (Figure 5a), recording visible light emission from this coupled system. The system was excited by scanning an electron beam across a coupled Al nanowire-Ag nanocube pair and collecting the light emitted from plasmonic bright modes, forming the CL image (Figure 5b-f). Bright modes are not spatially resolved. Without a Ag nanocube next to the nanowire, emission was mainly detected when the electron beam was positioned at the nanowire edges and defects (Figure S22). When the beam is scanned across the center of the nanowire (or the isolated nanocubes), local relative symmetry makes it difficult to excite the bright LSPR resonance, consistent with observations in other systems. 48,49 This is seen in Figure 5b, where the edges of the nanowire are brighter than the centers of the wire. Also seen in Figure 5b is the bright mode of either an Al or an alumina growth defect on the side of the nanowire as well as a small area of emission from the Al nanowire tip. Both appear dark when UV light is filtered from the image with a 400 nm long-pass filter (Figure 5c, d). This indicates that the majority of bright mode emission from these structures occurs at wavelengths shorter than visible light. For CL images filtered for 500 nm (Figure 5c) and 600 nm wavelength light detection (Figure 5d), the CL emission images of the Al nanowire appear more homogeneous than the panchromatic CL image (Figure 5b). We also collected spectra of the emitted CL at four select excitation points along the Al nanowire (Figure 5e, f). The two spectra obtained through direct e-beam excitation of the nanowire show very similar emission, supporting a broad peak

Nano Letters pubs.acs.org/NanoLett Letter

from ~500-600 nm (Figure 5e, f: green and red arrows and spectra). When a point near the end of the Al nanowire was excited, emission was centered at 500 nm (Figure 5e, f: orange arrow and spectrum). Direct e-beam excitation of the Ag cube directly adjacent to the Al nanowire shows a broad peak at ~550-600 nm (Figure 5e, f: blue arrow and spectrum). The broad CL spectrum from ~500-600 nm is likely due to combined Ag cube and Al nanowire tip emission. Coupling between the Al nanowire and Ag cube is strong enough that when the electron beam induces plasmon propagation along the nanowire, the Ag cube is also excited and results in the detection of the CL signal from ~550-600 nm. This propagated excitation of the Ag nanocube is best captured in the filtered 600 nm panchromatic CL image (Figure 5d). Changing the plasmonic emitter from a Ag cube to an Al NC also demonstrated similar remote excitation in CL mapping (Figure S24).

Al nanowires, nanomoustaches, and nanobars were colloidally synthesized by substituting Ti-based catalysts with V-centered compounds, slowing the rate of ligand-guided nanocrystal growth. Al nanowires demonstrate excellent optical properties due to their high degree of crystallinity. EELS plasmon mapping allows for visualization of the ultraviolet, visible, and IR modes supported by Al nanowires. EELS of the Al nanomoustache showcases its unique optical properties, which support a continuum of plasmonic modes. The coupling of these reduced-symmetry Al nanocrystals with other plasmonic metal structures was investigated. The coupling of Al nanowires with Au thin films resulted in the emergence of a quasi-bound state in a continuum resonance and the excitation of low-energy virtual film resonances in the near-infrared region of the spectrum. CL experiments confirmed that Al nanowires can remotely excite directly adjacent Ag nanocrystals, emitting visible light. With the combination of optical experiments performed, Al nanowires have been shown to support bright plasmon modes from the UV to the IR regions of the spectrum. The ambient stability and superior crystallinity of colloidally grown Al nanowires should lead to their incorporation into plasmonic systems in the future, energizing plasmonic optoelectronic applications.

ASSOCIATED CONTENT

Supporting Information

The Supporting Information is available free of charge at https://pubs.acs.org/doi/10.1021/acs.nanolett.4c00895.

Materials, experimental details, and supporting figures including additional simulations, SEM and TEM images, EELS and CL imaging and spectra, ICP-MS, EPR, and darkfield measurements. (PDF)

AUTHOR INFORMATION

Corresponding Authors

Naomi J. Halas — Laboratory for Nanophotonics, Rice University, Houston, Texas 77005, United States; Department of Chemistry, Department of Electrical and Computer Engineering, and Department of Physics and Astronomy, Rice University, Houston, Texas 77005, United States; orcid.org/0000-0002-8461-8494; Email: halas@rice.edu

Peter Nordlander – Laboratory for Nanophotonics, Rice University, Houston, Texas 77005, United States; Department of Electrical and Computer Engineering and Department of Physics and Astronomy, Rice University, Houston, Texas 77005, United States; oorcid.org/0000-0002-1633-2937; Email: nordland@rice.edu

Authors

- David Solti Laboratory for Nanophotonics, Rice University, Houston, Texas 77005, United States; Department of Chemistry, Rice University, Houston, Texas 77005, United States; occid.org/0000-0002-4687-565X
- Christian R. Jacobson Laboratory for Nanophotonics, Rice University, Houston, Texas 77005, United States; Department of Chemistry, Rice University, Houston, Texas 77005, United States; Occid.org/0000-0002-9578-8763
- J. Alexander Orion Yates Laboratory for Nanophotonics, Rice University, Houston, Texas 77005, United States; Department of Physics and Astronomy, Rice University, Houston, Texas 77005, United States; orcid.org/0000-0002-2555-2608
- Benjamin Franklin Hammel Renewable & Sustainable Energy Institute and Materials Science and Engineering Program, University of Colorado—Boulder, Boulder, Colorado 80309, United States; orcid.org/0000-0002-9155-9875
- Gopal Narmada Naidu Laboratory for Nanophotonics, Rice University, Houston, Texas 77005, United States; Department of Electrical and Computer Engineering and Applied Physics Graduate Program Smalley-Curl Institute, Rice University, Houston, Texas 77005, United States
- Catherine E. Arndt Laboratory for Nanophotonics, Rice University, Houston, Texas 77005, United States; Department of Electrical and Computer Engineering and Applied Physics Graduate Program Smalley-Curl Institute, Rice University, Houston, Texas 77005, United States; orcid.org/0000-0002-2041-8055
- Aaron Bayles Laboratory for Nanophotonics, Rice University, Houston, Texas 77005, United States; Department of Chemistry, Rice University, Houston, Texas 77005, United States; Occid.org/0000-0001-7396-7800
- Yigao Yuan Laboratory for Nanophotonics, Rice University, Houston, Texas 77005, United States; Department of Chemistry, Rice University, Houston, Texas 77005, United States; Occid.org/0000-0003-1385-2395
- Parmeet Dhindsa Laboratory for Nanophotonics, Rice University, Houston, Texas 77005, United States; Department of Chemistry, Rice University, Houston, Texas 77005, United States; orcid.org/0000-0003-0711-4492
- Jessica T. Luu Laboratory for Nanophotonics, Rice University, Houston, Texas 77005, United States; Research and Leadership Enabling Discoveries in Chemical Nanoscience Research Experience for Undergraduates, Department of Chemistry, Rice University, Houston, Texas 77005, United States; Ocid.org/0000-0002-0015-4347
- Corbin Farr Laboratory for Nanophotonics, Rice University, Houston, Texas 77005, United States; Department of Chemistry, Rice University, Houston, Texas 77005, United States
- Gang Wu Division of Hematology-Oncology Department of Internal Medicine, The University of Texas McGovern Medical School, Houston, Texas 77030, United States;

 occid.org/0000-0001-6803-0853
- Henry O. Everitt Department of Electrical and Computer Engineering, Rice University, Houston, Texas 77005, United States; [®] orcid.org/0000-0002-8141-3768

Ah-Lim Tsai – Division of Hematology-Oncology Department of Internal Medicine, The University of Texas McGovern Medical School, Houston, Texas 77030, United States

Sadegh Yazdi — Renewable & Sustainable Energy Institute and Materials Science and Engineering Program, University of Colorado—Boulder, Boulder, Colorado 80309, United States; Occid.org/0000-0002-3470-9398

Complete contact information is available at: https://pubs.acs.org/10.1021/acs.nanolett.4c00895

Notes

The authors declare no competing financial interest.

ACKNOWLEDGMENTS

D.S. thanks E. Akerboom, M. W. Knight, and J. B. Lassiter for their input on using CL instrumentation. D.S. thanks L. Yuan and A. Ogundare for their preparation of the Au films. This work was supported by the Robert A. Welch Foundation under grant no. C-1220 (N.J.H.) and C-1222 (P.N.), the AFOSR under grant no. FA9550-15-1-0022 (N.J.H.), and the National Science Foundation (NSF) under grant no. 2117903 (S.Y.). S.Y. and B.F.H. acknowledge support from the STROBE NSF Science & Technology Center, grant no. DMR-1548924. D.S. gratefully acknowledges support by the Department of Defense (DoD) through its National Defense Science and Engineering Graduate fellowship (NDSEG). C.E.A. and B.F.H. were supported by the NSF through the Graduate Research Fellowship Program (NSF-GRFP) under grant nos. 1842494 and DGE 2040434, respectively. The authors acknowledge the use of Electron Microscopy Center (EMC) at Rice University and the Facility for Electron Microscopy of Materials at the University of Colorado at Boulder (CU FEMM, RRID: SCR 019306).

REFERENCES

- (1) Kim, J.; Lee, H.-C.; Kim, K.-H.; Hwang, M.-S.; Park, J.-S.; Lee, J. M.; So, J.-P.; Choi, J.-H.; Kwon, S.-H.; Barrelet, C. J.; Park, H.-G. Photon-triggered nanowire transistors. *Nat. Nanotechnol.* **2017**, *12* (10), 963–968.
- (2) Lee, J. S.; Farmakidis, N.; Wright, C. D.; Bhaskaran, H. Polarization-selective reconfigurability in hybridized-active-dielectric nanowires. *Science Advances* **2022**, *8* (24), No. eabn9459.
- (3) Colinge, J.-P.; Lee, C.-W.; Afzalian, A.; Akhavan, N. D.; Yan, R.; Ferain, I.; Razavi, P.; O'Neill, B.; Blake, A.; White, M.; Kelleher, A.-M.; McCarthy, B.; Murphy, R. Nanowire transistors without junctions. *Nat. Nanotechnol.* **2010**, *5* (3), 225–229.
- (4) Liao, L.; Lin, Y.-C.; Bao, M.; Cheng, R.; Bai, J.; Liu, Y.; Qu, Y.; Wang, K. L.; Huang, Y.; Duan, X. High-speed graphene transistors with a self-aligned nanowire gate. *Nature* **2010**, *467* (7313), 305–308.
- (5) Hu, Y.; Chen, K.; Li, Y.-L.; He, J.-Y.; Zhang, K.-S.; Liu, T.; Xu, W.; Huang, X.-J.; Kong, L.-T.; Liu, J.-H. Morphology-tunable WMoO nanowire catalysts for the extremely efficient elimination of tetracycline: kinetics, mechanisms and intermediates. *Nanoscale* **2019**, *11* (3), 1047–1057.
- (6) Mao, J.; Chen, W.; He, D.; Wan, J.; Pei, J.; Dong, J.; Wang, Y.; An, P.; Jin, Z.; Xing, W.; Tang, H.; Zhuang, Z.; Liang, X.; Huang, Y.; Zhou, G.; Wang, L.; Wang, D.; Li, Y. Design of ultrathin Pt-Mo-Ni nanowire catalysts for ethanol electrooxidation. *Science Advances* **2017**, 3 (8), No. e1603068.
- (7) Wang, F.; Li, C.; Chen, H.; Jiang, R.; Sun, L.-D.; Li, Q.; Wang, J.; Yu, J. C.; Yan, C.-H. Plasmonic Harvesting of Light Energy for Suzuki Coupling Reactions. *J. Am. Chem. Soc.* **2013**, *135* (15), 5588–5601.
- (8) Zhang, Y.; Chu, W.; Foroushani, A. D.; Wang, H.; Li, D.; Liu, J.; Barrow, C. J.; Wang, X.; Yang, W. New Gold Nanostructures for Sensor Applications: A Review Materials [Online], 2014; pp 5169–5201.

- (9) Chen, W.; Peng, Q.; Li, Y. Alq3 Nanorods: Promising Building Blocks for Optical Devices. *Adv. Mater.* **2008**, 20 (14), 2747–2750.
- (10) Kolwas, K.; Derkachova, A. Impact of the Interband Transitions in Gold and Silver on the Dynamics of Propagating and Localized Surface Plasmons. *Nanomaterials* **2020**, *10* (7), 1411.
- (11) Wang, H.; Tam, F.; Grady, N. K.; Halas, N. J. Cu Nanoshells: Effects of Interband Transitions on the Nanoparticle Plasmon Resonance. *J. Phys. Chem. B* **2005**, *109* (39), 18218–18222.
- (12) Knight, M. W.; Grady, N. K.; Bardhan, R.; Hao, F.; Nordlander, P.; Halas, N. J. Nanoparticle-Mediated Coupling of Light into a Nanowire. *Nano Lett.* **2007**, *7* (8), 2346–2350.
- (13) Akimov, A. V.; Mukherjee, A.; Yu, C. L.; Chang, D. E.; Zibrov, A. S.; Hemmer, P. R.; Park, H.; Lukin, M. D. Generation of single optical plasmons in metallic nanowires coupled to quantum dots. *Nature* **2007**, *450* (7168), 402–406.
- (14) Fang, Y.; Li, Z.; Huang, Y.; Zhang, S.; Nordlander, P.; Halas, N. J.; Xu, H. Branched Silver Nanowires as Controllable Plasmon Routers. *Nano Lett.* **2010**, *10* (5), 1950–1954.
- (15) Fang, Y.; Wei, H.; Hao, F.; Nordlander, P.; Xu, H. Remote-Excitation Surface-Enhanced Raman Scattering Using Propagating Ag Nanowire Plasmons. *Nano Lett.* **2009**, *9* (5), 2049–2053.
- (16) Huang, Y.; Fang, Y.; Zhang, Z.; Zhu, L.; Sun, M. Nanowire-supported plasmonic waveguide for remote excitation of surface-enhanced Raman scattering. *Light: Science & Applications* **2014**, 3 (8), e199–e199.
- (17) Lee, S. J.; Moskovits, M. Remote Sensing by Plasmonic Transport. *J. Am. Chem. Soc.* **2012**, *134* (28), 11384–11387.
- (18) Zhang, Z.; Deckert-Gaudig, T.; Deckert, V. Label-free monitoring of plasmonic catalysis on the nanoscale. *Analyst* **2015**, 140 (13), 4325–4335.
- (19) Quan, L. N.; Kang, J.; Ning, C.-Z.; Yang, P. Nanowires for Photonics. *Chem. Rev.* **2019**, *119* (15), 9153–9169.
- (20) Jacobson, C. R.; Solti, D.; Renard, D.; Yuan, L.; Lou, M.; Halas, N. J. Shining Light on Aluminum Nanoparticle Synthesis. *Acc. Chem. Res.* **2020**, *53* (9), 2020–2030.
- (21) Zhou, L.; Zhang, C.; McClain, M. J.; Manjavacas, A.; Krauter, C. M.; Tian, S.; Berg, F.; Everitt, H. O.; Carter, E. A.; Nordlander, P.; Halas, N. J. Aluminum Nanocrystals as a Plasmonic Photocatalyst for Hydrogen Dissociation. *Nano Lett.* **2016**, *16* (2), 1478–1484.
- (22) Knight, M. W.; King, N. S.; Liu, L.; Everitt, H. O.; Nordlander, P.; Halas, N. J. Aluminum for Plasmonics. *ACS Nano* **2014**, *8* (1), 834–840.
- (23) Coenen, T.; Polman, A. Energy-Momentum Cathodoluminescence Imaging of Anisotropic Directionality in Elliptical Aluminum Plasmonic Bullseye Antennas. *ACS Photonics* **2019**, *6* (2), 573–580.
- (24) Chen, Y.; Wang, Y.; Zhu, S.; Chen, C.; Danner, V. A.; Li, Y.; Dai, J.; Li, H.; Fu, K. K.; Li, T.; Liu, Y.; Hu, L. One-Step, Catalyst-Free, Scalable in Situ Synthesis of Single-Crystal Aluminum Nanowires in Confined Graphene Space. ACS Appl. Mater. Interfaces 2019, 11 (6), 6009–6014.
- (25) Benson, J.; Boukhalfa, S.; Magasinski, A.; Kvit, A.; Yushin, G. Chemical Vapor Deposition of Aluminum Nanowires on Metal Substrates for Electrical Energy Storage Applications. *ACS Nano* **2012**, *6* (1), 118–125.
- (26) Thøgersen, A.; Jensen, I. J. T.; Belle, B. D.; Stange, M.; Reinertsen, V. M.; Kjeldstad, T.; Prytz, Ø.; Monakhov, E.; Kepaptsoglou, D. Plasmonic properties of aluminium nanowires in amorphous silicon. *J. Phys.: Condens. Matter* **2023**, *35*, 065301.
- (27) Singh, M.; Wang, J.; Tian, M.; Zhang, Q.; Pereira, A.; Kumar, N.; Mallouk, T. E.; Chan, M. H. W. Synthesis and Superconductivity of Electrochemically Grown Single-Crystal Aluminum Nanowires. *Chem. Mater.* **2009**, *21* (23), 5557–5559.
- (28) Clark, B. D.; Jacobson, C. R.; Lou, M.; Yang, J.; Zhou, L.; Gottheim, S.; DeSantis, C. J.; Nordlander, P.; Halas, N. J. Aluminum Nanorods. *Nano Lett.* **2018**, *18* (2), 1234–1240.
- (29) Clark, B. D.; Lou, M.; Nordlander, P.; Halas, N. J. Aluminum Nanocrystals Grow into Distinct Branched Aluminum Nanowire Morphologies. *Nano Lett.* **2020**, *20* (9), 6644–6650.

- (30) Clark, B. D.; Jacobson, C. R.; Lou, M.; Renard, D.; Wu, G.; Bursi, L.; Ali, A. S.; Swearer, D. F.; Tsai, A.-L.; Nordlander, P.; Halas, N. J. Aluminum Nanocubes Have Sharp Corners. *ACS Nano* **2019**, *13* (8), 9682–9691.
- (31) Yuan, L.; Lou, M.; Clark, B. D.; Lou, M.; Zhou, L.; Tian, S.; Jacobson, C. R.; Nordlander, P.; Halas, N. J. Morphology-Dependent Reactivity of a Plasmonic Photocatalyst. *ACS Nano* **2020**, *14* (9), 12054–12063.
- (32) Dhindsa, P.; Solti, D.; Jacobson, C. R.; Kuriakose, A.; Naidu, G. N.; Bayles, A.; Yuan, Y.; Nordlander, P.; Halas, N. J. Facet Tunability of Aluminum Nanocrystals. *Nano Lett.* **2022**, 22 (24), 10088–10094.
- (33) Jacobson, C. R.; Wu, G.; Alemany, L. B.; Naidu, G. N.; Lou, M.; Yuan, Y.; Bayles, A.; Clark, B. D.; Cheng, Y.; Ali, A.; Tsai, A.-L.; Tonks, I. A.; Nordlander, P.; Halas, N. J. A Dual Catalyst Strategy for Controlling Aluminum Nanocrystal Growth. *Nano Lett.* **2022**, 22 (13), 5570–5574.
- (34) Medford, A. J.; Vojvodic, A.; Hummelshøj, J. S.; Voss, J.; Abild-Pedersen, F.; Studt, F.; Bligaard, T.; Nilsson, A.; Nørskov, J. K. From the Sabatier principle to a predictive theory of transition-metal heterogeneous catalysis. *J. Catal.* **2015**, *328*, 36–42.
- (35) Yazdi, S.; Daniel, J. R.; Large, N.; Schatz, G. C.; Boudreau, D.; Ringe, E. Reversible Shape and Plasmon Tuning in Hollow AgAu Nanorods. *Nano Lett.* **2016**, *16* (11), 6939–6945.
- (36) Nicoletti, O.; de la Peña, F.; Leary, R. K.; Holland, D. J.; Ducati, C.; Midgley, P. A. Three-dimensional imaging of localized surface plasmon resonances of metal nanoparticles. *Nature* **2013**, *502* (7469), 80–84.
- (37) Rossouw, D.; Botton, G. A. Plasmonic Response of Bent Silver Nanowires for Nanophotonic Subwavelength Waveguiding. *Phys. Rev. Lett.* **2013**, *110* (6), 066801.
- (38) Rossouw, D.; Couillard, M.; Vickery, J.; Kumacheva, E.; Botton, G. A. Multipolar Plasmonic Resonances in Silver Nanowire Antennas Imaged with a Subnanometer Electron Probe. *Nano Lett.* **2011**, *11* (4), 1499–1504.
- (39) Mkhitaryan, V.; March, K.; Tseng, E. N.; Li, X.; Scarabelli, L.; Liz-Marzán, L. M.; Chen, S.-Y.; Tizei, L. H. G.; Stéphan, O.; Song, J.-M.; Kociak, M.; García de Abajo, F. J.; Gloter, A. Can Copper Nanostructures Sustain High-Quality Plasmons? *Nano Lett.* **2021**, *21* (6), 2444–2452.
- (40) Wang, C.; Yang, W.-C. D.; Raciti, D.; Bruma, A.; Marx, R.; Agrawal, A.; Sharma, R. Endothermic reaction at room temperature enabled by deep-ultraviolet plasmons. *Nat. Mater.* **2021**, *20* (3), 346–352.
- (41) Martin, J.; Kociak, M.; Mahfoud, Z.; Proust, J.; Gérard, D.; Plain, J. High-Resolution Imaging and Spectroscopy of Multipolar Plasmonic Resonances in Aluminum Nanoantennas. *Nano Lett.* **2014**, 14 (10), 5517–5523.
- (42) COMSOL Multiphysics, v. 5.4; COMSOL AB: Stockholm, Sweden.
- (43) McPeak, K. M.; Jayanti, S. V.; Kress, S. J. P.; Meyer, S.; Iotti, S.; Rossinelli, A.; Norris, D. J. Plasmonic Films Can Easily Be Better: Rules and Recipes. *ACS Photonics* **2015**, 2 (3), 326–333.
- (44) Zhukovsky, S. V.; Andryieuski, A.; Takayama, O.; Shkondin, E.; Malureanu, R.; Jensen, F.; Lavrinenko, A. V. Experimental Demonstration of Effective Medium Approximation Breakdown in Deeply Subwavelength All-Dielectric Multilayers. *Phys. Rev. Lett.* **2015**, *115* (17), 177402.
- (45) Johnson, P. B.; Christy, R. W. Optical Constants of the Noble Metals. *Phys. Rev. B* **1972**, *6* (12), 4370–4379.
- (46) Schinke, C.; Christian Peest, P.; Schmidt, J.; Brendel, R.; Bothe, K.; Vogt, M. R.; Kröger, I.; Winter, S.; Schirmacher, A.; Lim, S.; Nguyen, H. T.; MacDonald, D. Uncertainty analysis for the coefficient of band-to-band absorption of crystalline silicon. *AIP Advances* **2015**, 5 (6) 067168
- (47) Le, F.; Lwin, N. Z.; Steele, J. M.; Käll, M.; Halas, N. J.; Nordlander, P. Plasmons in the Metallic Nanoparticle—Film System as a Tunable Impurity Problem. *Nano Lett.* **2005**, *5* (10), 2009—2013. (48) Ringe, E.; DeSantis, C. J.; Collins, S. M.; Duchamp, M.; Dunin-Borkowski, R. E.; Skrabalak, S. E.; Midgley, P. A. Resonances of

- nanoparticles with poor plasmonic metal tips. Sci. Rep. 2015, 5 (1), 17431.
- (49) Edwards, P. R.; Sleith, D.; Wark, A. W.; Martin, R. W. Mapping Localized Surface Plasmons within Silver Nanocubes Using Cathodoluminescence Hyperspectral Imaging. *J. Phys. Chem. C* **2011**, *115* (29), 14031–14035.